Theoretical studies on the kinetics and dynamics of the $BeH^+ + H_2O$ reaction: Comparison with experiment

Jiaqi Li[1,2], Zhao Tu[2,3], Haipan Xiang[2,4], Yong Li,[1,*] Hongwei Song,[2,*]

[1]College of Physical Science and Technology, Huazhong Normal University, Wuhan 430079, China

[2]State Key Laboratory of Magnetic Resonance and Atomic and Molecular Physics, Innovation Academy for Precision Measurement Science and Technology, Chinese Academy of Sciences, Wuhan 430071, China

[3]School of Chemical and Environmental Engineering, Hubei Minzu University, Enshi 445000, China

[4]School of Physics and Electronics, Hunan University, Changsha 410082, China

[*]Corresponding author: yongli@mail.ccnu.edu.cn and hwsong@wipm.ac.cn

Abstract

The reaction of BeH^+ with background gas H_2O may play a role in qubit loss for quantum information processing with Be^+ as trapped ions, and yet its reaction mechanism has not been well understood until now. In this work, a globally accurate, full-dimensional ground-state potential energy surface (PES) for the $BeH^+ + H_2O$ reaction was constructed by fitting a total of 170,438 ab initio energy points at the level of RCCSD(T)-F12/aug-cc-pVTZ using the fundamental invariant-neural network method. The total root-mean-square error of the final PES was 0.178 kcal mol^{-1}. For comparison, quasi-classical trajectory calculations were carried out on the PES at the experimental temperature of 150 K. The obtained thermal rate constant and product branching ratio of the $BeD^+ + H_2O$ reaction agreed quite well with experimental results. In addition, the vibrational state distributions and energy disposals of the products were calculated and rationalized by the sudden vector projection model.

I. Introduction

Reactions between ions and neutral molecules widely exist in interstellar media, plasma and combustion, especially in low-temperature gas-phase environments.[1-10] Much effort has been made to study their energetics, kinetics and dynamics in the past several decades.[11-17] The long-range attractive interaction between ion charge and other neutral atoms or molecules was recognized to usually give rise to large reactive scattering cross sections at low or ultralow temperatures (or collision energies).[4, 18] If the colliders are captured by a deep potential well and form long-lived intermediate, the reaction often behaves as statistical due to significant energy randomization, which can be reliably described by capture theories,[19, 20] such as the Langevin capture theory.[21] Recently, it has, however, been found that the submerged barrier, straddling the pre- and post-saddle point (SP) wells in a number of ion-molecule reactions, exerts some control on the reactivity, resulting in non-statistical behavior. [9, 13, 22, 23]

The gas-phase ion-molecule reaction between beryllium hydride ion (BeH^+) and water molecule (H_2O) has attracted some attention in recent years due to its possible role in qubit loss.[24-26] Metal ions such as Be^+, Mg^+, Ca^+, Sr^+, Ba^+, and Yb^+ were used to carry quantum bits for quantum information processing.[27, 28] Be^+, as the lightest particle listed above, has unique advantages in providing a high frequency of motion to reduce gate time. Using the trapped Be^+ to host qubits has been proved to have a high-fidelity rate.[29] However, there also exist some faults for Be^+. Chemical reactions between Be^+ and the background gases, such as H_2 and H_2O, lead to qubit loss, as

observed by experiments performed in ultrahigh vacuum.[30, 31] Using an ion trap-integrated high-resolution time-of-flight mass spectrometer (TOF-MS), Yang et al. found that Be^+ first reacts with H_2 to form BeH^+, and then BeH^+ reacts with H_2O to form $BeOH^+$, which was supposed to be the dominant way for qubit loss.[24, 26] The reaction pathways were also determined at low temperatures by isotopically substituting BeH^+ by BeD^+ and only the double displacement product $BeOH^+$ was observed at ~ 150 K.[26]

The energetics of the $BeH^+ + H_2O$ reaction has been investigated by using the explicitly correlated restricted coupled cluster singles, doubles, and perturbative triples (RCCSD(T)-F12) method with the augmented correlation-consistent polarized triple zeta (AVTZ) basis set.[26] In addition to the exothermic double displacement reaction pathway, two more pathways were determined, including the nearly thermoneutral Be abstraction pathway and the endothermic H abstraction pathway. For the double displacement pathway to form H_2 and $BeOH^+$, there exists a submerged barrier of -39.20 kcal mol^{-1} with respect to the reactant asymptote, flanked by two deep ion-dipole wells. For the Be abstraction pathway to form Be and H_3O^+, two shallow wells are separated by a moderate submerged barrier of -7.45 kcal mol^{-1}. Although the reaction pathways have been determined by high-level ab initio method, the underlying reaction mechanisms were not fully unveiled. This work aims to develop an *ab initio* based globally accurate potential energy surface (PES) for the $BeH^+ + H_2O$ reaction and carry out dynamics and kinetics calculations on the PES at

the experimental temperature. The calculated thermal rate constant and product branching ratio will then be compared with recent experimental results.

II. Potential energy surface

The Born-Oppenheimer PES is of central importance in the field of molecular spectroscopy, reaction dynamics and kinetics. Most theoretical studies in the field were carried out on highly accurate PESs that were developed by fitting a large number of high-level ab initio energy points. The permutation invariance with respect to identical particles was usually enforced by implementing different techniques.[32-34] To build a global PES for the title reaction, the energy gap of sampled configurations should cover about 115 kcal mol^{-1}, i.e., from -80 to 35 kcal mol^{-1} with respect to the reactant asymptote, according to the energetics based on earlier high-level electronic structure calculations.[26] On the other hand, the farthest separation of reactants or products on the PES should be long enough to accurately describe long-range interactions, which is taken as 30 Å here. The PES of the $BeH^+ + H_2O$ reaction is constructed as follows.

The geometries of stationary points along the minimum energy path (MEP) are firstly optimized at the level of RCCSD(T)-F12/AVTZ using the software Molpro 2012.[35] A batch of grids are generated along the MEP and the direction perpendicular to the MEP and the energy of each reserved grid point is required to be lower than a pre-set value. Considering that the topography of interaction region is generally more

complex than the asymptotic regions, dense grids are used in the interaction region and sparse grids are used in the asymptotic region. Direct dynamics (ADMP) at the level of B3LYP/6-31G are then run from these grid points to sample more configurations using the software Gaussian 09.[36] The initial kinetic energy in direct dynamics is set to be low since some of the initial configurations have relatively high potential energies. The configurations obtained from the ADMP sampling have to be screened by the European criterion. The Euclidean distance is defined as $\chi = \sqrt{\sum_{i=1}^{10}|r_i - r_i'|^2}$, where r_i and r_i' represent the bond lengths of the existing configuration and the new configuration, respectively. The permutationally equivalent points are also included in the screening. The Euclidean distance in the interaction region is $\chi = 0.35$ Å, and gradually becomes larger as the two reactants or products get away from each other. The Euclidean distance is taken as $\chi = 0.59$ Å when the separation of reactants or products is up to 30 Å. After screening, 23,875 configurations satisfy the criterion and constitute the initial dataset.

The fundamental invariant-neural network (FI-NN) method is then employed to generate a raw PES by fitting the initial dataset.[37] The raw PES is generally crude and possibly contains artificial wells. Quasi-classical trajectories (QCT)[38] are then launched on the raw PES from different initial conditions, such as different vibration state, rotational state and translational energy, to sample more configurations. Both the European criterion and the average root mean square error of each configuration between several fitted PESs are used to select the sampled data points. The average

root mean square error is defined as $error = \sqrt{\sum_{i=1}^{n}(E_i - \bar{E})^2}$, in which n is the number of fitted PESs, E_i is the predicted potential energy of the i^{th} PES, and $\bar{E}$ is the average value over the n fitted PESs. The European distance varies from 0.15 Å to 0.27 Å from the interaction region to the asymptotic region. The screened configurations will be added to the raw dataset. The procedure has to be repeated several times to achieve a satisfactory level. In the end, the dataset contains a total of 170,438 data points.

To give a good asymptotic behavior for the fitted PES, the bond lengths are transformed into the Morse-like variables by $R_{morse} = \exp(-r/\alpha)$, in which r denotes the bond length.[39] It should be noted that the value of α should be carefully tested when there exist strong long-range interactions for the target systems. α is taken as 2.5 in this work. The Morse-like variables are then converted into fundamental invariant polynomials (FIs). The architecture of the neural network employed is 20-30-50-1, namely 20 FIs in the input layer, 30 and 50 neurons in the first and second hidden layers and one predicted energy in the output layer, giving a total of 2231 parameters. The root mean square error (RMSE), defined as $RMSE = \sqrt{\sum_{i=1}^{N_{data}}(E_{fit} - E_{ab\ initio})^2 / N_{data}}$, is used to evaluate the quality of each fitting. In the training, the data set is randomly divided into two groups: 95% of the points as the training set and 5% as the validating set. To diminish random errors, the final PES is built by averaging three best fitted PESs, resulting in a total RMSE of 0.178 kcal mol^{-1}.

III. Quasi-classical trajectory method

QCT method has been proved to be reasonably accurate in a wide range of polyatomic reactions although it has inherent drawbacks such as the inability to take into account quantum effects and the leakage of zero-point energy (ZPE). In this work, QCT calculations are performed by using the software VENUS 96.[40]

The integral cross section of the reaction at a specific temperature (or collision energy) is calculated by

$$\sigma(T) = \pi {b_{max}}^2 \frac{N_r}{N_{tot}}, \quad (1)$$

where N_{tot} is the number of total trajectories, N_r is the number of reactive trajectories. b_{max} is the maximum impact parameter, which is determined using small batches of trajectories with trial values and sampled by $b = R^{1/2} b_{max}$. R is a uniform random number in [0, 1]. The relative statistical error is defined as $\Delta = \sqrt{(N_{tot} - N_r)/N_{tot}N_r}$.

The differential cross section is computed by

$$\frac{d\sigma}{d\Omega} = \frac{\sigma P_r(\theta)}{2\pi sin(\theta)}, \quad (2)$$

where the scattering angle θ is defined as

$$\theta = cos^{-1}\left(\frac{\vec{v}_i \cdot \vec{v}_f}{|\vec{v}_i||\vec{v}_f|}\right), \quad (3)$$

in which $\vec{v}_i = \vec{v}_{BeH^+} - \vec{v}_{H_2O}$ and $\vec{v}_f = \vec{v}_{BeOH^+} - \vec{v}_{H_2}$ denote the initial and final relative velocities. $P_r(\theta)$ is normalized reaction probability at the scattering angle θ.

The thermal rate coefficient at temperature T is given by

$$k(T) = \left(\frac{8k_BT}{\pi\mu}\right)^{1/2}\sigma, \quad (4)$$

where μ is the reduced mass between the reactants, k_B is the Boltzmann constant. The initial rovibrational energies of the two reactants and the collision energy are sampled according to the Boltzmann and Maxwell-Boltzmann distributions, respectively.

For the diatomic product molecule H_2 (or HD in the isotopic substitution reaction), its vibrational state is determined by the Einstein-Brillouin-Keller semiclassical quantization of the action integral, as implemented in the software VENUS 96. In contrast, the determination of the vibrational state for polyatomic product molecule is not straightforward. The normal mode analysis (NMA) method[41-43] is employed in this work to calculate the vibrational state distribution of the product $BeOH^+$. To minish the effect of the harmonic approximation in NMA calculations, the coordinates and momenta are extracted from a specific step of each trajectory that demands the lowest potential energy for the corresponding geometry within the last several vibrational period of the product molecule.[44-48] Since energy in classical mechanics is not quantized, binning of trajectories is usually necessary to confer a "quantum spirit" on classical action number. Two binning methods, histogram binning (HB)[38] and energy-based Gaussian binning (1GB),[49-51] are employed to yield product quantum states. As mentioned above, the ZPE leakage is an inherent defect for classical mechanics. However, if one discards the trajectories that don't satisfy the ZPE constraint, the statistics is sometimes seriously disturbed.

Considering that it is still an open question, we do not apply any ZPE constraint in the calculations.

To compare with experimental measurement,[26] the collision energy and ro-vibrational states are sampled at 150 K. The trajectories are launched from a reactant separation of 28 Å and stopped when products or reactants move apart up to 28 Å for reactive or non-reactive trajectories. In the modified software, the reactive or nonreactive event will be checked only if the separation of the two approaching reactants is firstly smaller than 2.5 Å. The time step is set as 0.035 fs, conserving the energy better than 0.004 kcal mol^{-1} in the propagation. 150,000 trajectories are run, resulting in a relative statistical error of below 0.4 %.

IV. Results and discussion

The energies, geometry structures and harmonic frequencies of the stationary points along the MEPs on the fitted PES are calculated using the software POLYRATE 9.7.[52] Figure 1 shows the schematic diagram of the reaction paths, together with the geometries of the stationary points. The reaction paths are close to those determined by Yang et al.[26] except that the highly endothermic hydrogen abstraction path is absent. Clearly, if BeH^+ attacks H_2O by the Be-end, the reaction is more likely to proceed by the double displacement reaction pathway to form $BeOH^+$ and H_2. However, if BeH^+ attacks H_2O by the H-end, it prefers to produce Be and H_3O^+ by the hydrogen abstraction pathway. The ab initio energy at the level of

RCCSD(T)-F12/aug-cc-pVTZ, the fitted value on the PES and the ZPE corrected value of each stationary point are given in the figure as well. The fitted energy agrees well with the corresponding ab initio value. Most of the difference between them are smaller than 0.1 kcal mol^{-1}.

The optimized geometries of stationary points on the PES are listed in Table 1 and compared with ab initio results. The difference of bond length between fitted and *ab initio* values is smaller than 0.015 Å and the angle difference is less than 2°. Table 2 compares the harmonic frequencies of the stationary points on the PES with ab initio values. The difference is exclusively smaller than 80 cm^{-1}. The small difference between the fitted and ab initio values implies that the stationary points, no matter the geometry and the frequency, are well reproduced by the fitted PES. The distribution of the fitting errors of the sampled data points is presented in Fig. 2. Most of them are distributed in between -1.5 and 1.5 kcal mol^{-1}, with a few error points falling outside. As expected, the sampled data points with relatively large errors are mostly distributed in the high energy region.

Figure 3 shows the 2D contours of the PES for the hydrogen abstraction channel on the upper panel and the double displacement channel on the lower panel. They are plotted as a function of the breaking and forming bonds with other coordinates fixed at the geometry of the corresponding SP. Inserts enlarge the contours near the SPs. The fitted PES is smooth and there do not exist any artificial wells. The pre- and

post-SP wells and the submerged barrier along each reaction path are clearly displayed in the figure.

The MEPs of the two reaction channels on the PES are determined by the software POLYRATE 9.7 in mass-weighted Cartesian coordinates with a step size of 5.0×10^{-5} amu$^{1/2}$ Å, as shown in Fig. 4. The reaction coordinate s is defined as the signed distance from the corresponding SP ($s = 0$), with $s > 0$ representing the product side and $s < 0$ referring to the reactant side. It can be seen that the potential energy varies smoothly along with the reaction coordinate for both reaction paths, further verifying the smoothness of the fitted PES. To check the prediction accuracy, some configurations along the MEP were selected to carry out ab initio calculations at the level of RCCSD(T)-F12/aug-cc-pVTZ. For the double displacement reaction pathway, as shown in the lower panel, the optimized MEP on the PES agrees perfectly well with ab initio one. For the hydrogen abstraction pathway shown in the upper panel, the agreement is slightly poor in the asymptotic region but still acceptable. The vibrational adiabatic potential curves are also presented in the figure. There exists a kink in the post-SP region for the hydrogen abstraction adiabatic potential curve. In contrast, the double displacement adiabatic potential curve is much smoother.

With the PES in hand, trajectories are launched at the temperature of 150 K to simulate the TOF-MS experiment.[26] In the experiment, the reaction of the BeD^+ + H_2O reaction was observed to produce only $BeOH^+$， with assumed co-product of HD. The theoretical calculations under similar conditions find that nearly all launched

reactive trajectories form the products $BeOH^+$ and HD as well, whose percentage reaches 99.79%, as listed in Table 2. By contrast, the products Be and H_2DO^+ produced by the hydrogen abstraction path, and the isotopologue products $BeOD^+$ and H_2, accounting for less than 0.3%, are inaccessible at the temperature of 150 K. By analyzing the reactive trajectories to form the isotopologue products $BeOD^+$ and H_2, it is found that some of them proceed by the triple displacement channel while the rest occur by such a path, the colliders are firstly trapped in the MIN2 well along the hydrogen abstraction pathway, followed by the rotation of OH_3 moiety, then move down to the double displacement pathway and are trapped in the MIN3 well, and finally dissociate into $BeOD^+$ and H_2. The calculated thermal rate constant for the $BeD^+ + H_2O \rightarrow BeOH^+ + HD$ reaction is 4.0×10^{-9} $cm^3molecule^{-1}s^{-1}$, as shown in Table 2, is in good consistent with the experimental value of $(3.5 \pm 2) \times 10^{-9}$ $cm^3molecule^{-1}s^{-1}$. The good agreement between theoretical and experimental results further validates the accuracy of the newly developed PES.

The calculated differential cross sections for the $BeD^+ + H_2O \rightarrow BeOH^+ + HD$ reaction are shown in the upper panel of Fig. 5. The products are scattered in both forward and backward directions without any obvious bias, a typical characteristic of barrier-less complex-forming reactions. The distribution of scattering angles indicates that the double displacement reaction at T = 150 K is dominated by the indirect mechanism, apparently due to the existence of the deep pre- and post-SP wells. The lower panel exhibits the correlations between the impact parameter and the scattering

angle. As expected, the products are isotropically scattered at each specific impact parameter. The nearly symmetric forward-backward differential cross section suggests the existence of a long-lived intermediate complex, which has sufficient time to explore the reaction phase space and thus possibly erases all memory from the reactants. The energy is expected to redistribute among all available modes of motion, namely a statistical distribution.

The calculated vibrational state distributions of the products HD and $BeOH^+$ for the $BeD^+ + H_2O$ reaction are presented in Fig. 6. Since the HB and 1GB methods yield similar results, the following discussions are based on the 1GB results. The product HD is largely populated in the ground vibrational state. As the excitation energy increases, the population of HD in each vibrational state monotonically decreases. The three quantum numbers (ν_1, ν_2, ν_3) in the parentheses of the lower panel denote excitations in the Be-O stretching mode, the degenerate bending mode of $BeOH^+$, and O-H stretching mode, respectively. The corresponding frequencies are 1569.89 cm^{-1}, 387.40 cm^{-1}, and 3997.03 cm^{-1}. Note that ν_2 is the sum of excitations in the two degenerate bending modes. Obviously, the product $BeOH^+$ is formed in a wide region of vibrational states without any dominant population states. The populations in the fundamental and ground states of the bending mode are a little higher. As the excitation energy increases, the product $BeOH^+$ slightly prefers to be formed in the combination bands of the fundamental of the bending mode and several low-lying vibrationally excited states of the Be-O stretching mode. The O-H

stretching mode in the product $BeOH^+$ is not visibly excited. Therefore, the vibrational state distribution of $BeOH^+$ has some non-statistical characteristics, portending an insufficiently long lifetime of the intermediate complexes.

To unveil the energy flow in the reaction, the product energy disposals of the $BeD^+ + H_2O \rightarrow HD + BeOH^+$ reaction are determined as well, as shown in Fig. 7. f_v, f_r and f_t represent the fractions of the available energy released as the vibrational energy, the rotational energy and the relative translational energy of the products HD and $BeOH^+$. 31.9 % of the available energy is released as the vibrational energy of $BeOH^+$, followed by the relative translational energy, the vibrational energy of HD and the rotational energy of $BeOH^+$, with a percentage of around 20%. The rotational energy of HD has a relatively small fraction with a value of 10.32%. The fractions indicate that the available energy is more favorable to flow into the vibrational modes of both products and yet is unfavorable to channel into the rotational mode of the product HD, implying that the energy randomization of the intermediate complexes is not fully completed.

As mentioned above, for bimolecular reactions with submerged barriers, the submerged SP sometimes exerts some control on the reaction, resulting in non-statistical behavior.[9, 13, 22, 23, 46, 53, 54] In this case, the sudden vector projection (SVP) model,[55] which attributes the energy flow to the coupling of the product mode with the reaction coordinate at the transition state, could be used to explain the product vibrational state distribution and energy disposal. Table 4 lists the calculated

SVP values of the product vibrational modes and the translational mode. The stretching mode of HD has the largest projection of 0.83, followed by the translational mode of 0.52 and the O-Be stretching mode of 0.16. The O-H stretching mode and the degenerate bending mode of $BeOH^+$, have very weak coupling with the reaction coordinate. The predictions are in partially agreement with the QCT results, such as the negligible excitation of the O-H stretching mode in the product $BeOH^+$ and the biased product energy disposal to the product vibrational and translational modes. However, it should also be noted that the bending mode is highly excited in the product BeOH. This obviously cannot be explained by the SVP model. The discrepancy is thought to be reasonable since the effect of the submerged SP is not dominant. Most of the reactive trajectories occur by the complex-forming mechanism. The SVP values for the other path $BeD^+ + H_2O \rightarrow Be^+ + H_2DO^+$ are given in the same table for reference.

V. Conclusions

In this work, a full-dimensional, globally accurate PES for the $BeH^+ + H_2O$ reaction was constructed by fitting a total of 170,438 ab initio energy points at the level of RCCSD(T)-F12/AVTZ. The flexible fundamentally invariant-neural network method was employed in the fitting, giving a RMSE of 0.178 kcal mol^{-1}. The energies, geometries and harmonic frequencies of the stationary points along the two minimum energy paths were well reproduced by the fitted PES. Quasiclassical

trajectory calculations were carried out on the PES under the experimental condition. The measured thermal rate constant of the $BeD^+ + H_2O$ reaction and product branching ratio were well reproduced by the theoretical calculations. The differential cross section has a nearly symmetric forward-backward distribution, implying the dominance of the barrier-less complex-forming mechanism. The product vibrational state distribution of the reaction showed some non-statistical characteristics, indicating that the energy randomization of the intermediate complexes formed in the reaction was not fully finished. The submerged saddle point was supposed to exert some control on the reaction and thus the dynamical behavior can be partially rationalized by the SVP model.

Conflicts of interest

There are no conflicts of interest to declare.

Acknowledgements

This work is supported by the National Natural Science Foundation of China under the Grant No. 21973109.

Table 1: Bond lengths (in angstrom) and angles (in degree) of the stationary points along the minimum energy paths of the $BeH^+ + H_2O$ reaction. The atom labels are given in Fig. 1.

Species	Method	R_{Be1H2}(Å)	R_{H2H3}(Å)	R_{H3O4}(Å)	R_{O4H5}(Å)	$\theta_{H3H2Be1}$(°)	θ_{O4H3H2}(°)	θ_{H5O4H3}(°)	$\varphi_{O4H3H2Be1}$(°)	$\varphi_{H5O4H3Be1}$(°)
$BeH^+ + H_2O$	*Ab initio*[a]	1.314			0.959			104.430		
	PES[b]	1.315			0.959			104.420		
MIN1	*Ab initio*[a]	1.344	2.703	0.961	0.961	163.646	35.988	104.651	177.105	179.741
	PES[b]	1.349	2.692	0.962	0.962	163.551	37.608	104.784	180.000	180.000
SP1	*Ab initio*[a]	1.504	2.068	0.966	0.966	157.402	39.971	106.766	163.549	132.351
	PES[b]	1.506	2.064	0.966	0.966	156.992	40.204	106.526	167.010	130.697
MIN2	*Ab initio*[a]	2.066	1.659	0.974	0.974	146.790	35.691	110.349	179.895	123.707
	PES[b]	2.051	1.661	0.973	0.973	148.043	35.644	109.980	175.882	125.348
$Be+H_3O^+$	*Ab initio*[a]		1.617	0.976	0.976		34.067	111.887		
	PES[b]		1.617	0.976	0.976		34.131	111.738		
MIN3	*Ab initio*[a]	1.307	3.509	0.970	0.970	13.026	41.612	109.275	0.024	179.961
	PES[b]	1.307	3.511	0.970	0.970	13.012	41.588	109.201	0.000	180.000
SP2	*Ab initio*[a]	1.409	1.124	1.263	0.962	68.808	127.939	129.689	0.007	179.958
	PES[b]	1.408	1.127	1.260	0.962	68.830	127.851	130.128	0.000	179.999
MIN4	*Ab initio*[a]	1.612	0.779	2.922	0.952	76.014	82.339	172.338	0.152	179.388
	PES[b]	1.618	0.777	2.929	0.952	76.107	82.377	172.377	0.000	180.000
$BeOH^+ + H_2$	*Ab initio*[a]		0.742		0.953					
	PES[b]		0.742		0.953					

[a]RCCSD(T)-F12/aug-cc-pVTZ by Molpro2012, this work; [b]FI-NN PES, this work.

Table 2: Harmonic frequencies (in cm^{-1}) and energies (in kcal mol^{-1}) of stationary points along the minimum energy path of the $BeH^+ + H_2O$ reaction.

Species	Method	mode1	mode2	mode3	mode4	mode5	mode6	mode7	mode8	mode9
$BeH^+ + H_2O$	*Ab initio*[a]	3943.50	3833.62	2211.44	1647.44					
	PES[b]	3979.60	3860.80	2209.90	1637.90					
MIN1	*Ab initio*[a]	3914.60	3814.30	1952.54	1652.29	325.84	261.25	259.79	179.61	99.55
	PES[b]	3921.90	3772.40	1916.70	1657.00	324.60	238.00	237.10	180.20	152.60
SP1	*Ab initio*[a]	3850.30	3741.30	1638.65	915.93	756.91	650.66	416.15	396.90	-577.93
	PES[b]	3854.30	3694.80	1666.00	934.00	752.60	665.80	422.20	412.90	-579.80
MIN2	*Ab initio*[a]	3744.33	3658.93	2457.29	1663.92	1614.38	968.46	432.93	340.60	269.34
	PES[b]	3775.60	3736.40	2465.30	1697.90	1667.50	959.40	444.00	349.60	276.30
$Be+H_3O^+$	*Ab initio*[a]	3703.30	3703.10	3603.35	1698.44	1697.29	887.71			
	PES[b]	3712.20	3712.20	3616.40	1746.30	1746.30	905.70			
MIN3	*Ab initio*[a]	3778.26	3712.07	2290.48	1682.24	857.39	765.59	441.03	340.53	317.27
	PES[b]	3783.10	3707.60	2283.00	1666.90	853.90	772.90	436.70	331.00	319.10
SP2	*Ab initio*[a]	3853.08	2192.28	1922.76	1261.10	1139.84	1130.54	649.18	120.96	-1730.19
	PES[b]	3877.80	2213.60	1928.90	1268.40	1149.20	1147.40	676.90	145.90	-1738.00
MIN4	*Ab initio*[a]	4008.45	3933.50	1598.70	1263.00	964.11	393.68	372.81	183.49	179.21
	PES[b]	4014.60	3950.90	1598.20	1226.50	953.40	365.10	359.30	182.10	151.00
$BeOH^+ + H_2$	*Ab initio*[a]	4401.09	3992.35	1566.44	392.93	392.19				
	PES[b]	4399.90	3997.03	1569.89	387.40	387.40				

[a]RCCSD(T)-F12/aug-cc-pVTZ by Molpro2012, this work; [b]FI-NN PES, this work.

Table 3: Comparison of experimental and theoretical product branching ratios ($\sigma_{BeOH^+}:\sigma_{BeOD^+}:\sigma_{H_2DO^+}$) and rate constants (in $cm^3molecule^{-1}s^{-1}$) of the BeD^+ + H_2O reaction at 150 K.

	Exp.	Theo.
Product branching ratio (%)	100:0:0	99.79:0.20:0.01
Rate constant	$(3.5 \pm 2) \times 10^{-9}$	4.0×10^{-9}

Table 4: Projections of reactant and the product vibrational modes on the reaction coordinate at the submerged saddle point.

	type	Vibrational frequency (cm^{-1})	SVP values
$HD + BeOH^+$	HD stretch	3810.88	0.83
	OBe stretch	1569.89	0.16
	in-plane bend	387.40	0.00
	out-of-plane bend	387.40	0.03
	OH stretch	3997.03	0.02
	Trans		0.52
$Be + H_2DO^+$	OH symmetric stretch	3650.98	0.05
	Umbrella	836.60	0.17
	OH asymmetric stretch	3712.24	0.00
	OD stretch	2676.04	0.90
	OH_2 bend	1721.39	0.20
	Deformation	1474.16	0.00
	Trans		0.33

References:

1. E. E. Ferguson, *Annu. Rev. Phys. Chem.*, 1975, **26**, 17-38.
2. W. D. Watson, *Acc. Chem. Res.*, 1977, **10**, 221-226.
3. D. Smith, *Chem. Rev.*, 1992, **92**, 1473-1485.
4. C.-Y. Ng, in *Adv. Chem. Phys.*, 1992, DOI: https://doi.org/10.1002/9780470141397.ch6, pp. 401-500.
5. J. Farrar, in *Springer Handbook of Atomic, Molecular, and Optical Physics*, ed. G. Drake, Springer New York, New York, NY, 2006, pp. 983-993.
6. N. S. Shuman, D. E. Hunton and A. A. Viggiano, *Chem. Rev.*, 2015, **115**, 4542-4570.
7. P. Manikandan, J. Zhang and W. L. Hase, *J. Phys. Chem. A*, 2012, **116**, 3061-3080.
8. J. Meyer and R. Wester, *Annu. Rev. Phys. Chem.*, 2017, **68**, 333-353.
9. Y. Wang, H. Song, I. Szabó, G. Czakó, H. Guo and M. Yang, *J. Phys. Chem. Lett.*, 2016, **7**, 3322-3327.
10. T. J. Millar, C. Walsh and T. A. Field, *Chem. Rev.*, 2017, **117**, 1765-1795.
11. I. Szabó, A. G. Császár and G. Czakó, *Chem. Sci.*, 2013, **4**, 4362.
12. Y. Xu, B. Xiong, Y. C. Chang and C.-Y. Ng, *Astrophys. J.*, 2018, **861**, 17.
13. H. Song, A. Li, H. Guo, Y. Xu, B. Xiong, Y. C. Chang and C. Y. Ng, *Phys. Chem. Chem. Phys.*, 2016, **18**, 22509-22515.
14. S. Rednyk, Š. Roučka, A. Kovalenko, T. D. Tran, P. Dohnal, R. Plašil and J. Glosík, *A&A*, 2019, **625**, A74.
15. T. Yang, A. Li, G. K. Chen, Q. Yao, A. G. Suits, H. Guo, E. R. Hudson and W. C. Campbell, *Sci Adv*, 2021, **7**, eabe4080.
16. J. Meyer, V. Tajti, E. Carrascosa, T. Győri, M. Stei, T. Michaelsen, B. Bastian, G. Czakó and R. Wester, *Nat. Chem.*, 2021, **13**, 977-981.
17. R. Wild, M. Notzold, M. Simpson, T. D. Tran and R. Wester, *Nature*, 2023, **615**, 425-429.
18. E. Carrascosa, J. Meyer and R. Wester, *Chem. Soc. Rev.*, 2017, **46**, 7498-7516.
19. H. Guo, *Int. Rev. Phys. Chem.*, 2012, **31**, 1-68.
20. A. Tsikritea, J. A. Diprose, T. P. Softley and B. R. Heazlewood, *J. Chem. Phys.*, 2022, **157**, 060901.
21. P. Langevin, *Ann. Chim. Phys.*, 1905, **5**, 245-288.
22. Y. Liu, H. Song, D. Xie, J. Li and H. Guo, *J. Am. Chem. Soc.*, 2020, **142**, 3331-3335.
23. L. Tian, H. Song and M. Yang, *Phys. Chem. Chem. Phys.*, 2021, **23**, 2715-2722.
24. T. Yang, A. Li, G. K. Chen, C. Xie, A. G. Suits, W. C. Campbell, H. Guo and E. R. Hudson, *J. Phys. Chem. Lett.*, 2018, **9**, 3555-3560.
25. G. K. Chen, C. Xie, T. Yang, A. Li, A. G. Suits, E. R. Hudson, W. C. Campbell and H. Guo, *Phys. Chem. Chem. Phys.*, 2019, **21**, 14005-14011.

26. T. Yang, B. Zhao, G. K. Chen, H. Guo, W. C. Campbell and E. R. Hudson, *New. J. Phys.*, 2021, **23**, 115004.
27. D. Nigg, M. Müller, E. A. Martinez, P. Schindler, M. Hennrich, T. Monz, M. A. Martin-Delgado and R. Blatt, *Science*, 2014, **345**, 302-305.
28. S. Debnath, N. M. Linke, C. Figgatt, K. A. Landsman, K. Wright and C. Monroe, *Nature*, 2016, **536**, 63-66.
29. J. P. Gaebler, T. R. Tan, Y. Lin, Y. Wan, R. Bowler, A. C. Keith, S. Glancy, K. Coakley, E. Knill, D. Leibfried and D. J. Wineland, *Phys. Rev. Lett.*, 2016, **117**, 060505.
30. D. J. Wineland, C. Monroe, W. M. Itano, D. Leibfried, B. E. King and D. M. Meekhof, *J Res Natl Inst Stand Technol*, 1998, **103**, 259-328.
31. M. McAneny, B. Yoshimura and J. K. Freericks, *Phys. Rev. A*, 2013, **88**, 043434.
32. C. Qu, Q. Yu and J. M. Bowman, *Annu. Rev. Phys. Chem.*, 2018, **69**, 151-175.
33. B. Jiang, J. Li and H. Guo, *J. Phys. Chem. Lett.*, 2020, **11**, 5120-5131.
34. S. Manzhos and T. Carrington, *Chem. Rev.*, 2021, **121**, 10187-10217.
35. H.-J. Werner, P. J. Knowles, G. Knizia, F. R. Manby and M. Schuetz, *Wiley Interdiscip. Rev. Comput. Mol. Sci.*, 2012, **2**, 242-253.
36. M. J. Frisch, G. W. Trucks, H. B. Schlegel, G. E. Scuseria, M. A. Robb, J. R. Cheeseman, G. Scalmani, V. Barone, G. A. Petersson, H. Nakatsuji, X. M. Li and others, *Gaussian 09, Revision B.01,* , Gaussian, Inc., Wallingford CT, 2009.
37. K. Shao, J. Chen, Z. Zhao and D. H. Zhang, *J. Chem. Phys.*, 2016, **145**, 071101.
38. D. G. Truhlar and J. T. Muckerman, in *Atom - Molecule Collision Theory: A Guide for the Experimentalist*, ed. R. B. Bernstein, Springer US, Boston, MA, 1979, DOI: 10.1007/978-1-4613-2913-8_16, pp. 505-566.
39. B. J. Braams and J. M. Bowman, *Int. Rev. Phys. Chem.*, 2009, **28**, 577-606.
40. W. L. Hase, R. J. Duchovic, X. Hu, A. Komornicki, K. F. Lim, D.-H. Lu, G. H. Peslherbe, K. N. Swamy, S. R. Vande Linde, A. Varandas, H. Wang and R. J. Wolf, *Quantum Chem. Program Exch. Bull.*, 1996, **16**, 43.
41. J. Espinosa-García, J. L. Bravo and C. Rangel, *J. Phys. Chem. A*, 2007, **111**, 2761-2771.
42. J. Espinosa-García and J. L. Bravo, *J. Phys. Chem. A*, 2008, **112**, 6059-6065.
43. J. C. Corchado and J. Espinosa-Garcia, *Phys. Chem. Chem. Phys.*, 2009, **11**, 10157-10164.
44. L. Ping, L. Tian, H. Song and M. Yang, *J. Phys. Chem. A*, 2018, **122**, 6997-7005.
45. L. Ping, Y. Zhu, A. Li, H. Song, Y. Li and M. Yang, *Phys. Chem. Chem. Phys.*, 2018, **20**, 26315-26324.
46. L. Tian, Y. Zhu, H. Song and M. Yang, *Phys. Chem. Chem. Phys.*, 2019, **21**, 11385-11394.

47. Y. Zhu, L. Tian, H. Song and M. Yang, *J. Phys. Chem. A*, 2020, **124**, 6794-6800.
48. Y. Zhang, X. Zhou and B. Jiang, *J. Phys. Chem. Lett.*, 2019, **10**, 1185-1191.
49. G. Czakó and J. M. Bowman, *J. Chem. Phys.*, 2009, **131**, 244302.
50. L. Bonnet and J. Espinosa-García, *J. Chem. Phys.*, 2010, **133**, 164108.
51. L. Bonnet, *Int. Rev. Phys. Chem.*, 2013, **32**, 171-228.
52. J. Zheng, J. L. Bao, R. Meana-Pañeda, S. Zhang, B. J. Lynch, J. C. Corchado, Y.-Y. Chuang, P. L. Fast, W.-P. Hu, Y.-P. Liu, G. C. Lynch, K. A. Nguyen, C. F. Jackels, A. F. Ramos, B. A. Ellingson, V. S. Melissas, J. Villà, I. Rossi, E. L. Coitiño, J. Pu and T. V. Albu, *POLYRATE, version 9.7*, Department of Chemistry and Supercomputing Institute, University of Minnesota, 2007.
53. H. Song, A. Li and H. Guo, *J. Phys. Chem. A*, 2016, **120**, 4742-4748.
54. M. C. Babin, M. DeWitt, J. A. Lau, M. L. Weichman, J. B. Kim, H. Song, H. Guo and D. M. Neumark, *Nat. Chem.*, 2023, **15**, 194-199.
55. H. Guo and B. Jiang, *Acc. Chem. Res.*, 2014, **47**, 3679-3685.

Figure captions

Fig. 1: Schematic diagram of the two reaction paths for the $BeH^+ + H_2O$ reaction. The ab initio energies of stationary points at the level of RCCSD(T)-F12/ aug-cc-pVTZ, the values of the fitted PES and the zero-point energy corrected values are shown below the corresponding geometries. All energies are given in kcal mol^{-1} and relative to the reactant asymptote.

Fig. 2: Distribution of fitting errors ($E_{\text{ab initio}}$-E_{fit}) of sampled data points as a function of the ab initio energy.

Fig. 3: (a) 2D contours of the PES for the $BeH^+ + H_2O \rightarrow Be + H_3O^+$ reaction as a function of the broken H-Be bond and the formed H-O bond with the other coordinates fixed at the geometry of the submerged saddle point; (b) 2D contours of the PES for the $BeH^+ + H_2O \rightarrow H_2 + BeOH^+$ reaction as a function of the broken H-Be bond and the formed Be-O bond. Inserts show the details of the PES near the submerged saddle points.

Fig. 4: Classical potential energy curve (V_{MEP}) and vibrational adiabatic potential curve (V_a^G) on the PES as a function of the reaction coordinate for the $BeH^+ + H_2O \rightarrow Be + H_3O^+$ reaction (upper panel) and the $BeH^+ + H_2O \rightarrow H_2 + BeOH^+$ reaction (lower panel). The corresponding ab initio energies (circles) along the minimum energy paths are given as well for comparison.

Fig. 5: Differential cross sections of the $BeD^+ + H_2O \rightarrow HD + BeOH^+$ reaction at 150 K (upper panel) and correlations between the impact parameter and the scattering angle (lower panel).

Fig. 6: Vibrational state distributions of the products HD and $BeOH^+$ for the $BeD^+ + H_2O \rightarrow HD + BeOH^+$ reaction at 150 K.

Fig. 7: Product energy Disposals of the $BeD^+ + H_2O \rightarrow HD + BeOH^+$ reaction at 150 K.

Fig. 1:

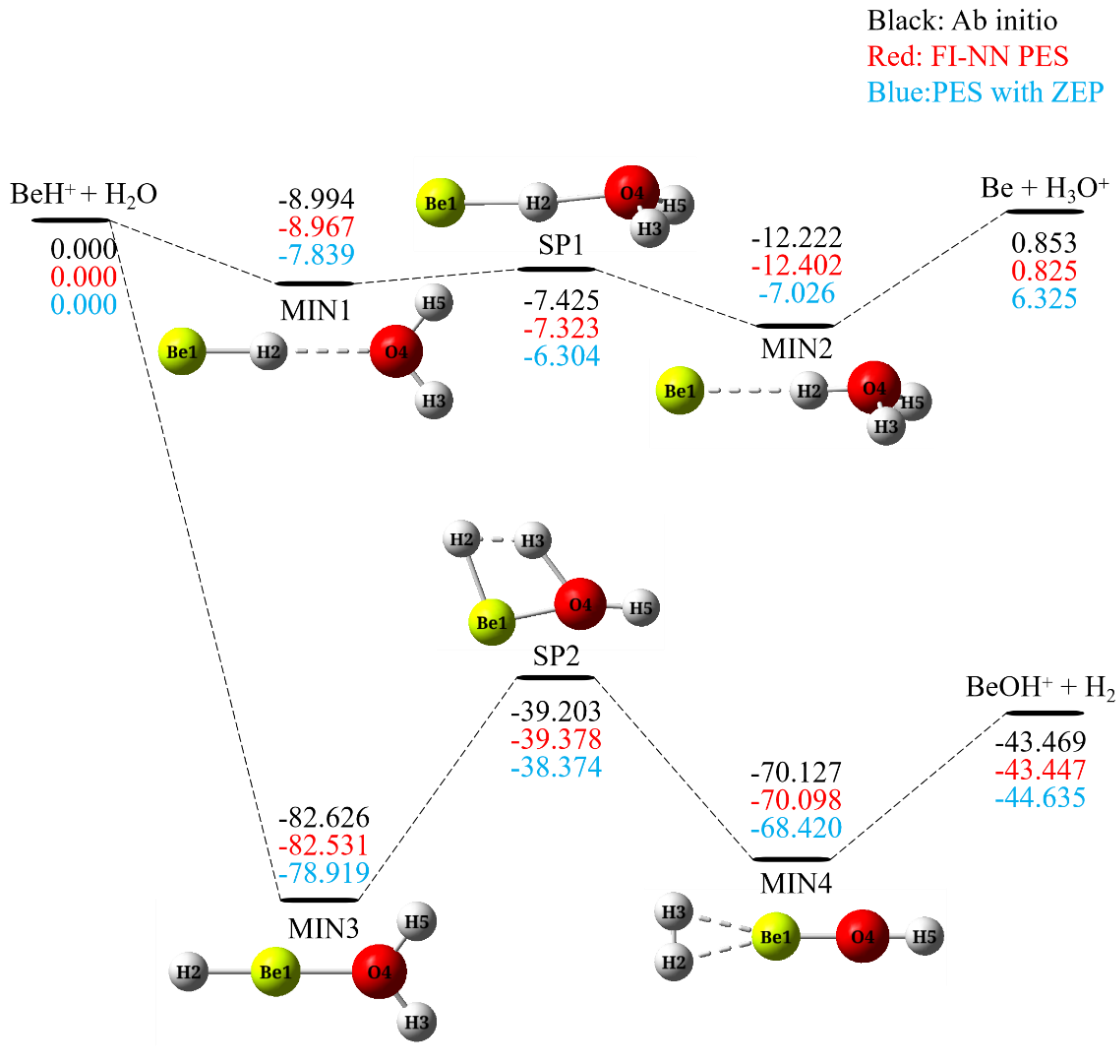
Black: Ab initio
Red: FI-NN PES
Blue:PES with ZEP
BeH⁺ + H₂O
0.000
0.000
0.000
-8.994
-8.967
-7.839
MIN1
SP1
-7.425
-7.323
-6.304
-12.222
-12.402
-7.026
MIN2
Be + H₃O⁺
0.853
0.825
6.325
SP2
-39.203
-39.378
-38.374
-82.626
-82.531
-78.919
MIN3
-70.127
-70.098
-68.420
MIN4
BeOH⁺ + H₂
-43.469
-43.447
-44.635

Fig. 2:

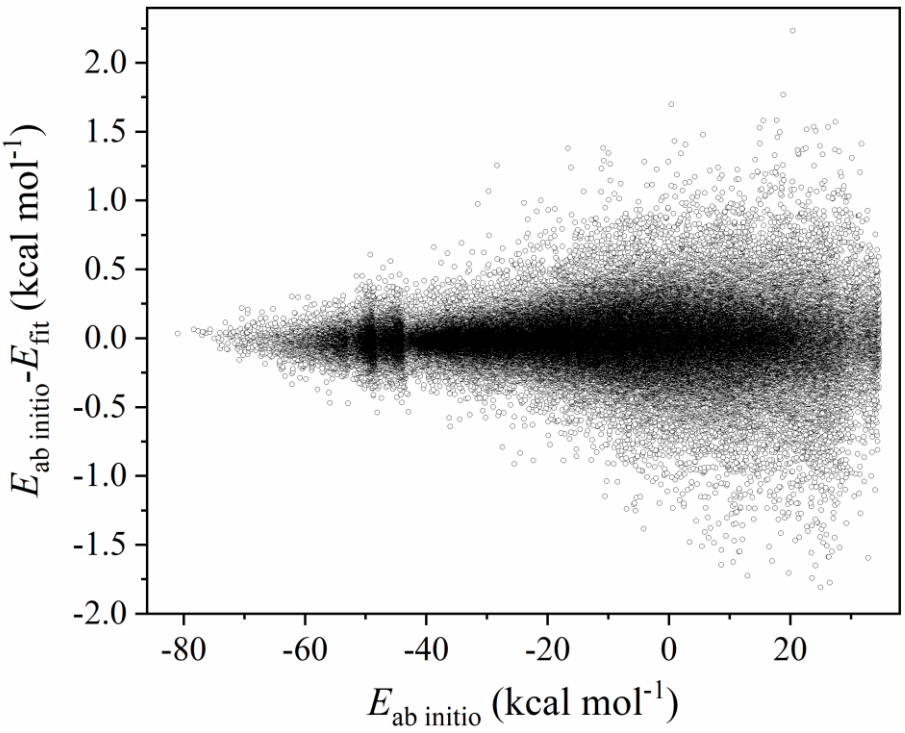
2.0
1.5
1.0
0.5
0.0
-0.5
-1.0
-1.5
-2.0
-80
-60
-40
-20
0
20
$E_{ab\ initio}$-E_{fit} (kcal mol^{-1})
$E_{ab\ initio}$ (kcal mol^{-1})

Fig. 3:

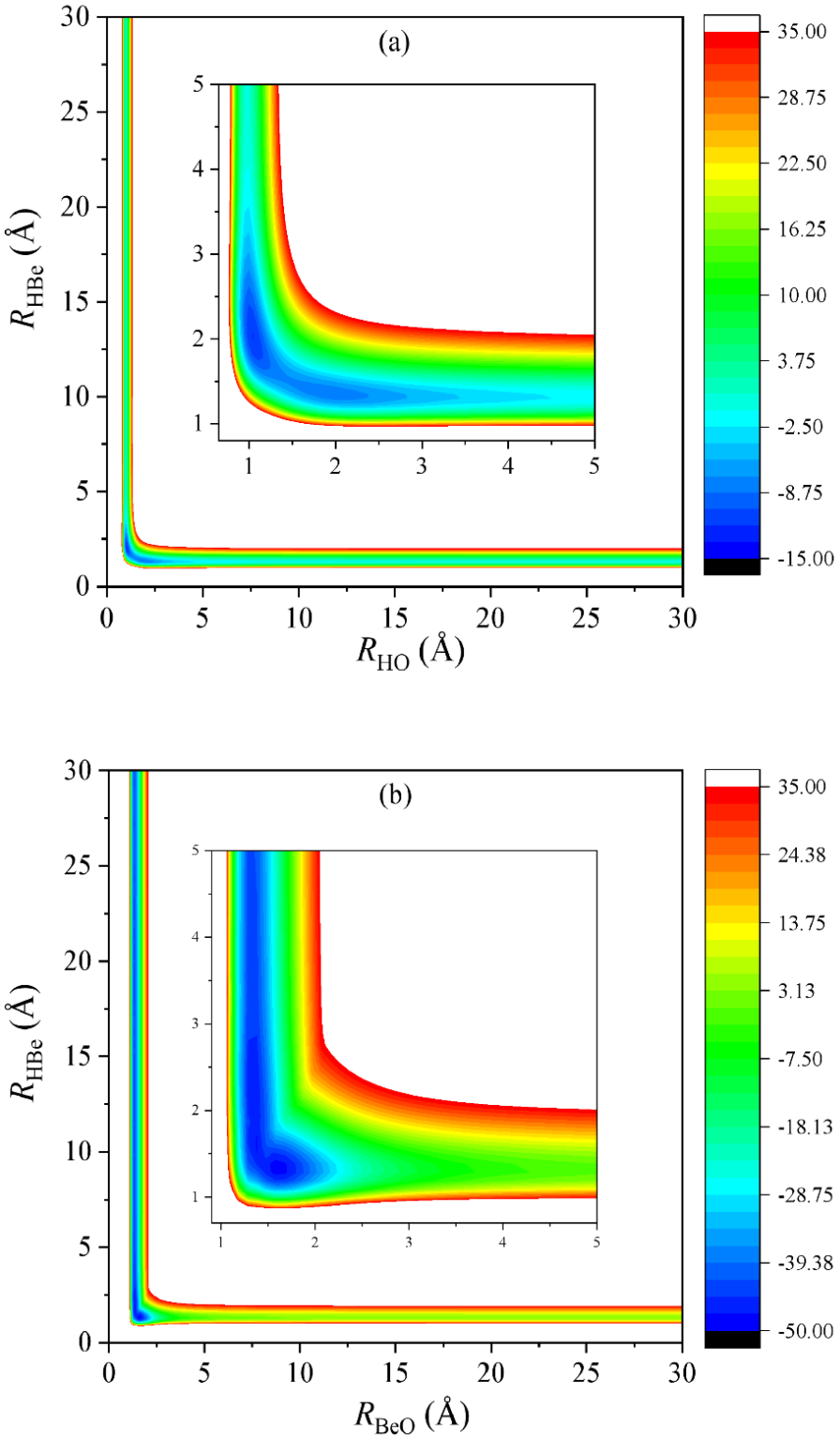
(a)
R_{HBe} (Å)
R_{HO} (Å)
35.00
28.75
22.50
16.25
10.00
3.75
-2.50
-8.75
-15.00
(b)
R_{HBe} (Å)
R_{BeO} (Å)
35.00
24.38
13.75
3.13
-7.50
-18.13
-28.75
-39.38
-50.00

Fig. 4:

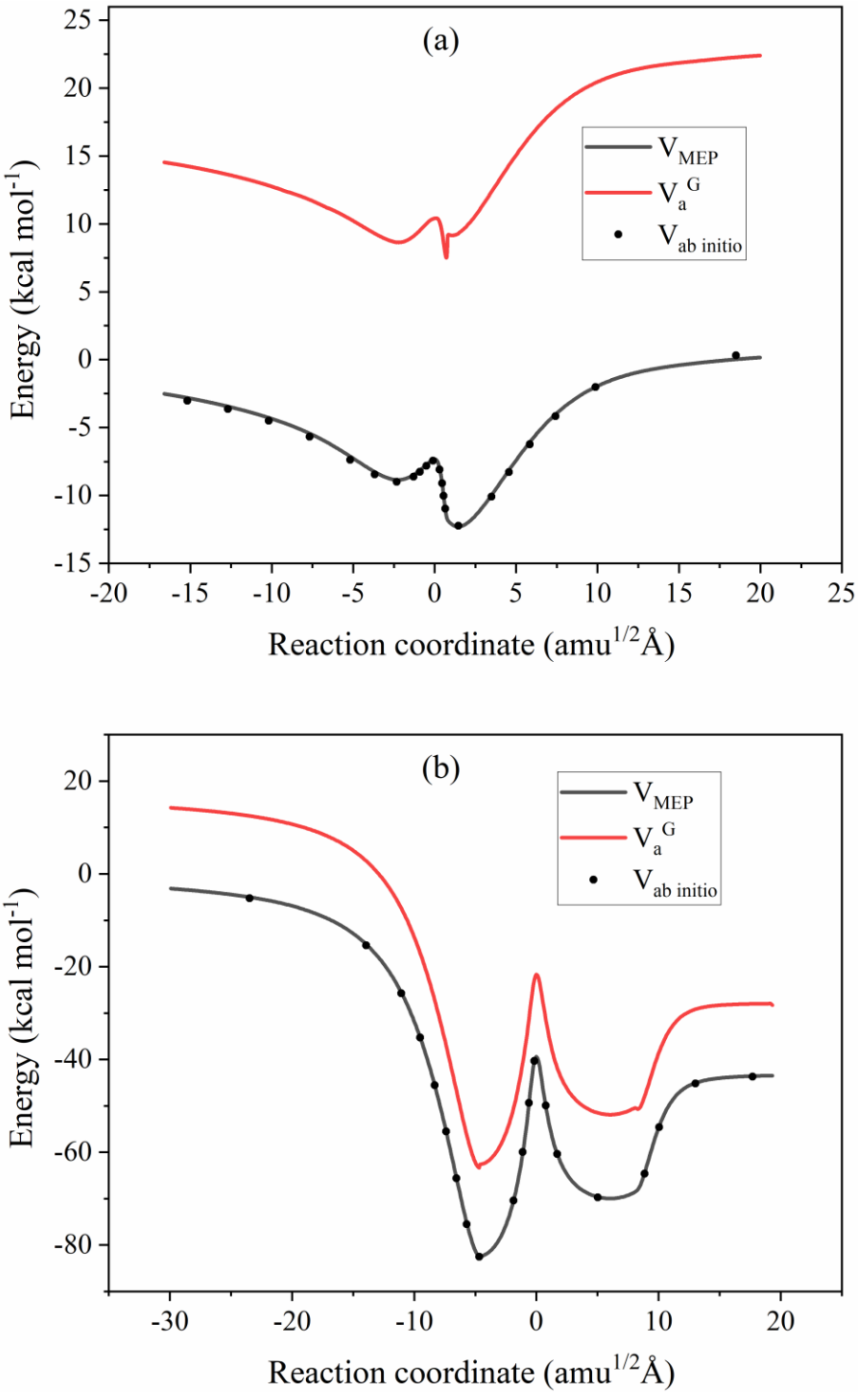
(a)
Energy (kcal mol-1)
Reaction coordinate (amu1/2Å)
VMEP
VaG
Vab initio
(b)
Energy (kcal mol-1)
Reaction coordinate (amu1/2Å)
VMEP
VaG
Vab initio

Fig. 5:

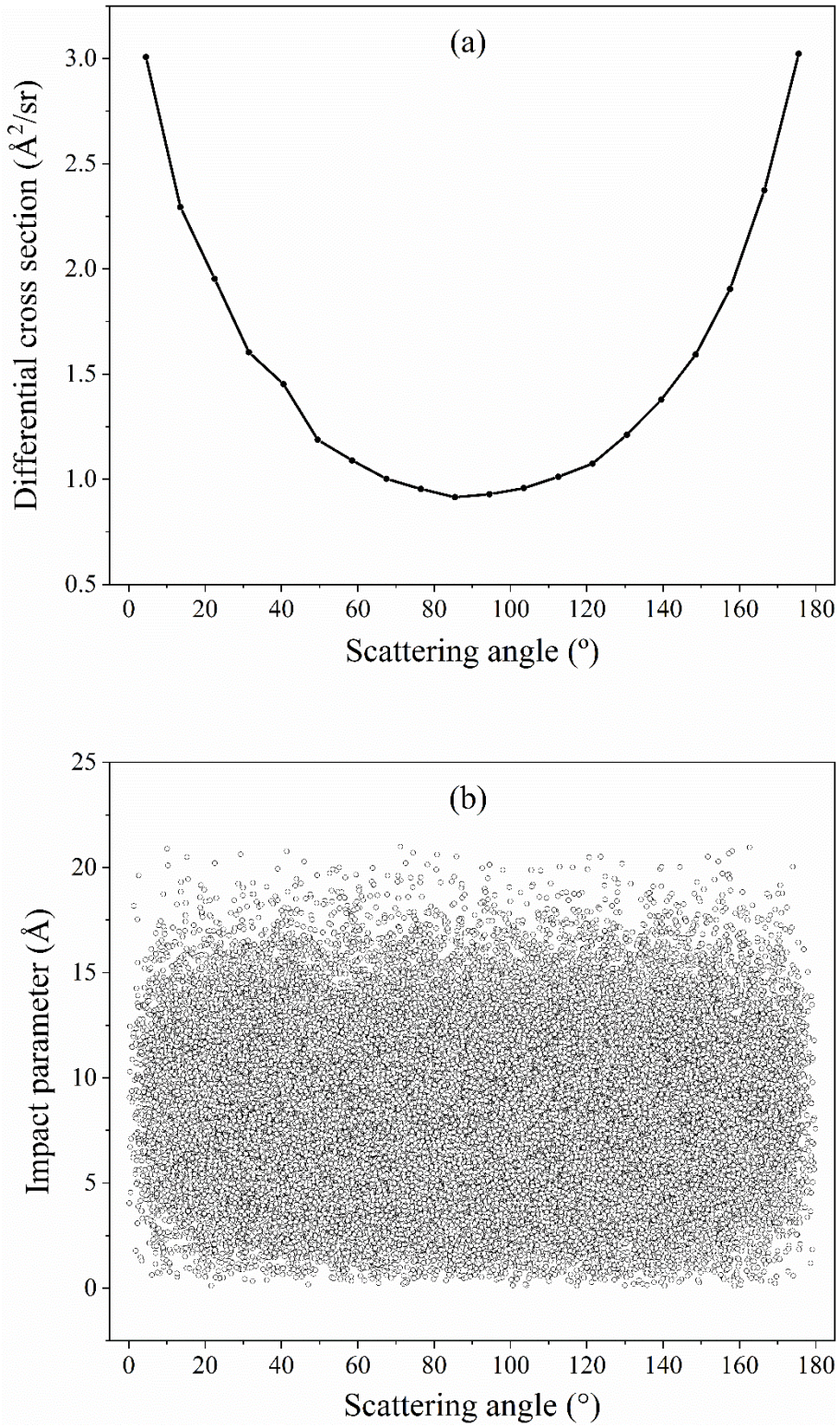
(a)
Differential cross section (Å²/sr)
3.0
2.5
2.0
1.5
1.0
0.5
0
20
40
60
80
100
120
140
160
180
Scattering angle (º)
(b)
Impact parameter (Å)
25
20
15
10
5
0
0
20
40
60
80
100
120
140
160
180
Scattering angle (°)

Fig. 6:

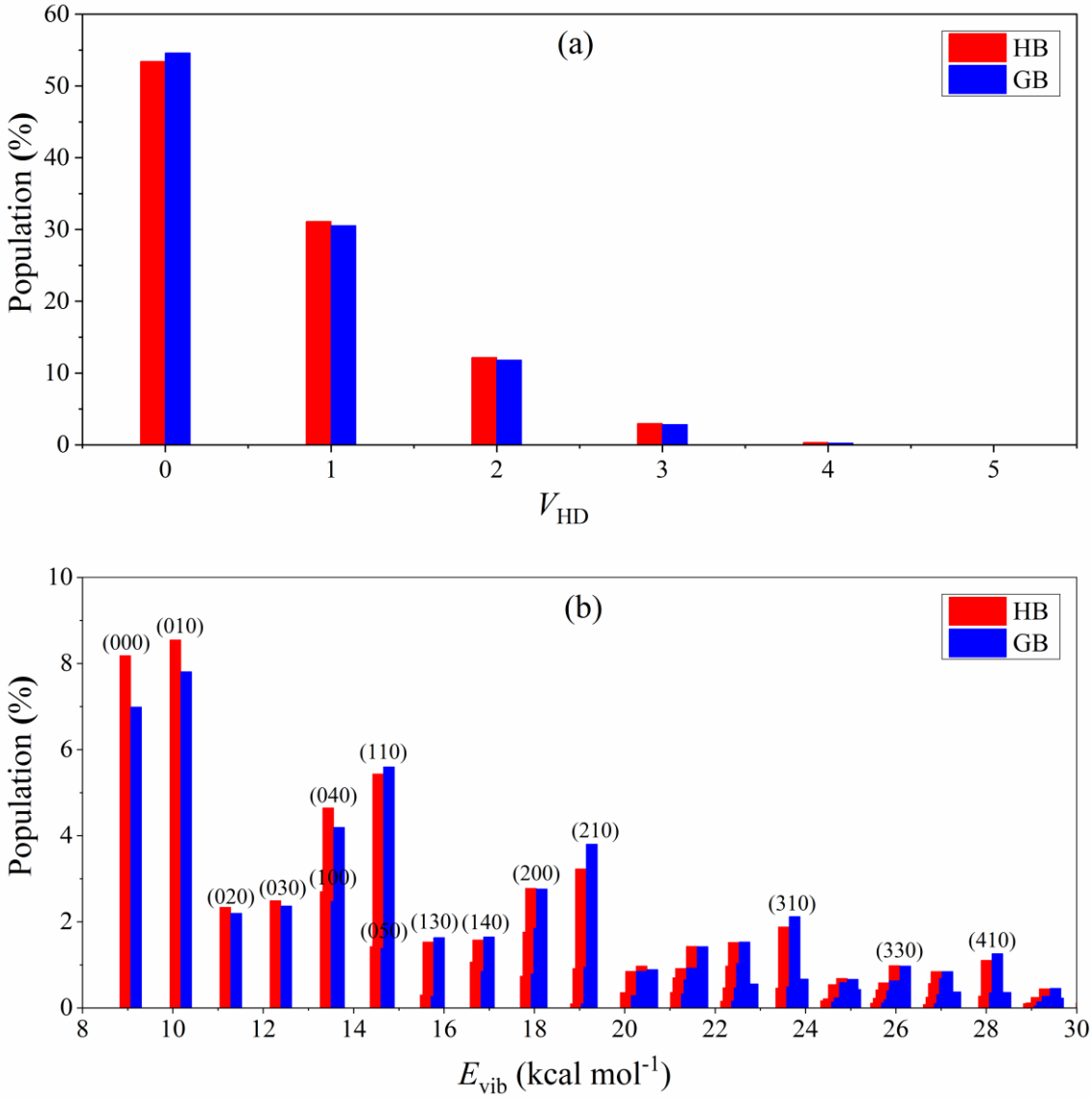
(a)
HB
GB
Population (%)
V_{HD}
(b)
HB
GB
Population (%)
(000)
(010)
(020)
(030)
(100)
(040)
(110)
(050)
(130)
(140)
(200)
(210)
(310)
(330)
(410)
E_{vib} (kcal mol^{-1})

Fig. 7: